CHARACTERIZING VORTICAL STRUCTURES IN THE LOWER LOG REGION OF THE ATMOSPHERIC BOUNDARY LAYER USING LARGE-SCALE PARTICLE TRACKING VELOCIMETRY

Giuseppe A. Rosi[1,*], Michael Sherry[1], Matthias Kinzel[2] and David E. Rival[1]
[1]Department of Mechanical Engineering, University of Calgary, Calgary, Canada *garosi@ucalgary.ca
[2]Graduate Aerospace Laboratories, California Institute of Technology, Pasadena, USA

ABSTRACT

A large-scale particle tracking velocimetry (LS-PTV) system has been developed as a means of quantifying coherent structures within the atmospheric boundary layer. The LS-PTV system resolves three-dimensional, Lagrangian tracks over a volume of approximately 16m^3. Mean velocity and Reynolds stresses have been validated and compared with wind-mast measurements and boundary-layer similarity formulations. The probability distributions for streamwise, spanwise and vertical velocity-fluctuation components agree with Gaussian distributions of equal variance. In contrast, the probability distributions for acceleration and vorticity are exponential and symmetric about zero. Thus, extreme acceleration events and vorticity events would be underpredicted by a Gaussian distribution. Finally, examples of particle paths exhibiting a high degree of swirl are presented, which are speculated to be signatures of large vortical structures.

1 INTRODUCTION

Given the limitations of laboratory-scale experiments, our understanding of neutral atmospheric boundary layers (ABLs) and their relation to canonical turbulent boundary layers (TBLs) remains incomplete. Lab-based tests such as the *Princeton Superpipe* have only recently achieved Reynolds numbers on the order of ABLs (McKeon & Morrison, 2007), and have been used mostly to explore the statistical properties of turbulence (Smits *et al.*, 2011). High Reynolds-number tests have shown that the mean-velocity profile and fluctuation statistics are nearly independent of Reynolds number (Marusic *et al.*, 2010*a*,*b*). However, there has been some marked dissimilarities between the statistics of low and high Reynolds-number tests. For instance, at a momentum-thickness Reynolds number of $Re_\theta = 16000$, the streamwise Reynolds stress begins exhibiting a secondary peak at the onset of the logarithmic region, while the streamwise energy spectra exhibits a secondary peak at wavelengths of 10δ (Fernholz & Finley, 1996; McKeon & Morrison, 2007). Both peaks become more pronounced with increasing Reynolds number, and have been attributed to *very large streamwise motions* with length-scales of roughly 10δ (Hutchins & Marusic, 2007).

The similarities in the turbulent coherent motions or *coherent structures* within ABLs and TBLs are also not well established. The aforementioned studies used point measurements rather than field velocimetry techniques to acquire data and therefore are incapable of quantifying the spatial characteristics of coherent structures. Studies that have used field velocimetry techniques to investigate coherent structures have identified the hairpin-vortex as a ubiquitous structure responsible for the salient features of TBL flow (Adrian, 2007). However, the low Reynolds numbers used by these studies makes their relevance to high Reynolds-number flows uncertain (Smits *et al.*, 2011). The existence of large hairpin vortices within ABLs has been speculated (Adrian, 2007), but the robustness of such structures in the presence of high shear remains tentative (Marusic *et al.*, 2010*b*). Furthermore, coherent structures have been shown to be affected significantly by Reynolds number even within the limited range investigated to date. For example, from particle image velocimetry (PIV) data taken along the streamwise wall-normal plane, Wu & Christensen (2006) observed that the ratio of retrograde-to-prograde vortices within a TBL grows with increasing Reynolds number in the range ($3870 \leq Re_\theta \leq 10730$). This runs contrary to classical hairpin-vortex theory, see Robinson (1991), which suggests that only prograde spanwise vortices should be present in the lower log region. Using Tomographic PIV, Schroeder *et al.* (2011) obtained three-dimensional visualizations of hairpin vortices, which in turn demonstrated that at even moderate Reynolds numbers ($Re_\theta = 2460$), hairpin vortices are increasingly asymmetrical with one of the hairpin legs exhibiting a maximum absolute vorticity 15% larger than the other. The increase in asymmetry observed by Schroeder *et al.* (2011) suggests that hairpin vortices deform from their classic shape at modest Reynold numbers. Such deformation would increase the occurrence of retrograde vortices, which is dependent on the orientation of hairpin vortices to the measurement plane.

The quantification of coherent structures within ABL flow remains challenging given the large boundary-layer thickness, $\delta \sim \mathscr{O}(1000\text{m})$. Coherent structures within ABLs and TBLs have only been compared qualitatively, and the use of conventional wind-mast data to quantify coherent structures within ABLs has severe limitations; see Scarabino *et al.* (2007), Rosi *et al.* (in press). Furthermore, investigations that have visualized coherent structures within ABLs have had to compromise between qualitatively measuring full-scale structures, as done in Hommema & Adrian (2003) via smoke visualizations of full-scale hairpin packets, and quantitative measurements within a small ($1\text{m} \times 0.5\text{m}$) field-of-view with PIV; see Morris *et al.* (2007).

Finally, the similarities between ABLs and canoni-

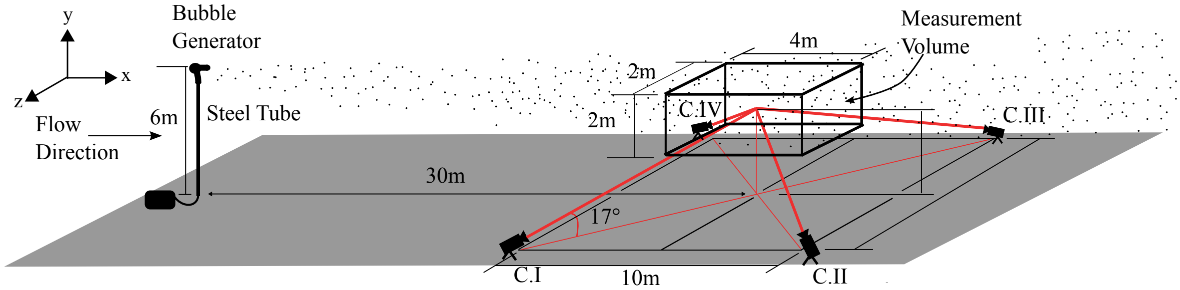

Figure 1: A schematic of the LS-PTV setup. The bubble generator is shown on the left, whereas the camera arrangement and the resultant measurement volume is shown on the right.

cal TBLs in regards to the vorticity and acceleration dynamics remain inadequately understood. This is primarily due to the application of point measurements in high Reynolds-number studies, which prevents one from calculating spatial derivatives of velocity. Thus, insight into the vorticity and acceleration dynamics of TBLs has only been gained at lower Reynolds numbers. For example, probability distributions of vorticity were measured by Balint *et al.* (1991) in a nominally zero-pressure-gradient TBL at $Re_\theta = 2685$. Also, Lagrangian accelerations have been studied by La Porta *et al.* (2001) for isotropic turbulence within a Taylor-microscale Reynolds number range of $200 \leq Re_\lambda \leq 970$ and also by Schroeder *et al.* (2011) for a TBL at $Re_\theta = 2460$. Both found the acceleration to be isotropic, such that the streamwise, spanwise and vertical components of acceleration exhibited nearly identical probability distributions.

To address the shortcomings of the aforementioned studies, a novel large-scale particle tracking velocimetry (LS-PTV) system that tracks the motion of small, fog-filled soap bubbles has been developed and deployed. The system is the first to produce fully three-dimensional quantitative measurements of coherent structures within the lower log region of the ABL. Furthermore, the system generates Lagrangian data, which is preferable when studying coherent structures as it ensures frame invariance. The manuscript begins by describing the LS-PTV system. This is then followed by a comparison between the mean LS-PTV data and data collected by a nearby wind mast as well as with an eddy-covariance system. The probability distributions of velocity fluctuations, acceleration, and vorticity are presented and compared with canonical TBL results. Lastly, particle paths that exhibit a high degree of swirl are presented. It is postulated that such paths are indicative of vortical motions.

2 EXPERIMENTAL SETUP

The LS-PTV measurements to be presented here were captured at a wind-measurement station northwest of the University of Calgary. The site is grassy and can be described as rural. Wind velocity and other meteorological data were simultaneously recorded by a nearby wind mast and eddy-covariance system. The wind mast is 50m tall and is equipped with five NRG#40 cup anemometers (CA) and five NRG200P wind vanes that provide ten-minute averages of data sampled at 1Hz. Furthermore, a three-component ultrasonic anemometer (Ultrasonic Anemometer 3D, Thies Clima) located at a height of 40m is used to determine the Reynolds stresses. Further details of the wind mast can be found in Rosi *et al.* (in press). To avoid interference, the LS-PTV apparatus was positioned approximately 70m from the wind mast. The eddy covariance system measured the friction velocity U_τ, and also provided an estimate of atmospheric stability. This system is further described in Hayashi *et al.* (2010).

The LS-PTV system is shown schematically in Figure 1. It consists of four bubble generators and their reservoirs mounted on a 6m-tall pole. The pole is tethered for stability. Fog is delivered to the bubble generators via a manifold system. Each bubble generator is individually triggered and produces fog-filled bubbles at a rate of ≈100–200 per minute. To track the bubbles, four digital video cameras (EOS-Rebel T3i, Canon) are positioned downstream of the bubble generators. Each camera is equipped with a 50mm focal length lens (AF-D f1.4, Nikkor). Videos are captured at 60Hz and at a resolution of 1280×720 pixels. The cameras are synchronized by a custom radio to infra-red remote. Images are extracted and processed using open-source PTV software (Lüthi *et al.*, 2009). The measurement volume is approximately 4m×2m×2m in the $x-$,$y-$ and $z-$directions. The data was rotated such that the $x-$, $y-$ and $z-$ axes are aligned with the streamwise, vertical and spanwise wind directions.

3 RESULTS & DISCUSSION

LS-PTV data was extracted from video footage captured on March 27, 2013 between 15:30 and 15:50. The system produces three-dimensional Lagrangian data of the tracked particles, including position, velocity, acceleration and vorticity. Although velocity measurements are achievable by point measurements, Lagrangian acceleration and vorticity are not. Furthermore, unlike LS-PTV, point measurements cannot capture the pathlines of the flow field. 2148 tracks were produced from the collected data. Several examples of tracks are shown in Figure 2.

The LS-PTV data is presented in the following section. First, the mean statistics of the LS-PTV data are compared to data from the wind mast and the eddy-covariance system. Probability distributions of velocity fluctuations, accelerations and vorticity are shown next.

3.1 Mean Statistics

To evaluate the measurement capabilities of the LS-PTV system, the mean velocity U, and Reynolds stresses $\overline{u'u'}$, $\overline{v'v'}$, and $\overline{u'v'}$ were compared to the wind mast and eddy-covariance system data. Mean-velocity measurements are shown in Figure 3. The wind-mast measurements are indicated by the red-square markers while the mean velocity measured by the LS-PTV system is indicated by the green-triangle marker. The red curve is a logarithmic wind profile given by $u(y) = (U_\tau/\kappa)\ln(y/y_0)$. Here $u(y)$ is the mean wind profile, κ is the von-Kármán constant, y is height, U_τ

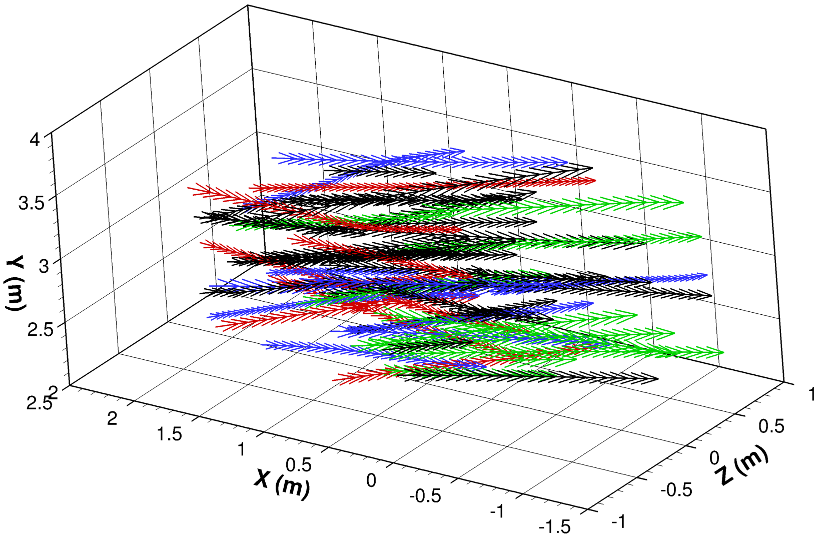

Figure 2: Examples of tracks produced by the LS-PTV system. The arrows along the path indicate the direction of the flow. The tracks are colored for sake of clarity.

is the friction velocity and y_0 is the roughness length. To construct the logarithmic profile in Figure 3, $y_0 = 0.03$m (WMO, 2008), which is typical of rural grassland, and U_τ is equal to the value measured by the eddy-covariance system. The horizontal bars represent the square root of the streamwise Reynolds stresses ($\sqrt{\overline{u'u'}}$). Figure 3 indicates that the mean velocity determined by the LS-PTV system agrees well with the logarithmic profile. The system can thus accurately measure the wind velocity. The LS-PTV system measures a larger streamwise Reynolds stress compared to the cup anemometers, which is likely caused by the proximity of the measurement volume to the ground.

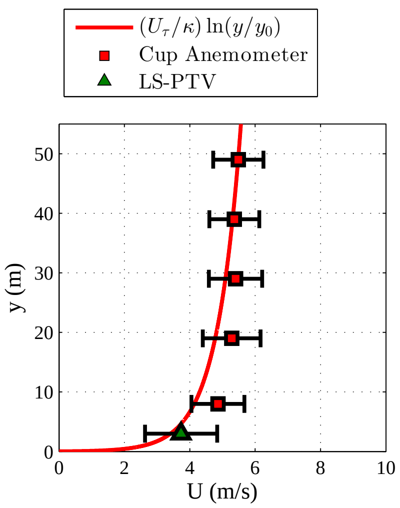

Figure 3: Mean-velocity measurements from the wind mast, eddy-covariance system and LS-PTV system. The red markers indicate measurements taken by the wind mast, while the green triangle represents the mean velocity measured by LS-PTV system. The red curve represents the profile $u(y) = (U_\tau/\kappa)\ln(y/y_0)$. Horizontal bars represent $\sqrt{\overline{u'u'}}$.

The streamwise, vertical and shear stresses ($\overline{u'u'}$, $\overline{v'v'}$ and $\overline{u'v'}$, respectively) measured by the LS-PTV system are compared to measurements taken by the ultrasonic anemometer and cup anemometers in Figure 4. The black curves in Figure 4(a) and 4(b) are Reynolds-stress similarity formulations developed in Marusic *et al.* (1997) and Kunkel & Marusic (2006). The black curve in Figure 4(c) represents the line $\overline{u'v'}/(U_\tau)^2 = -1$, which is valid within the logarithmic region of the ABL (Kaimal & Finnigan, 1994). The vertical and shear stresses measured by the LS-PTV system and the ultrasonic anemometer agree with the similarity formulations. However, there is some discrepancy between the similarity formulation for $\overline{u'u'}$ and the corresponding measurements. Aside from the measurements taken by the ultrasonic anemometer and the cup anemometer located at $y^+ = 1.4\times10^5$, all measurements of $\overline{u'u'}$ overshoot the similarity formulation. ABL measurements taken by Kunkel & Marusic (2006) agreed well with the similarity formulations during stable stratification conditions where the Obukhov length was measured as $60\text{m} \le L \le 90\text{m}$. In contrast, Kunkel & Marusic (2006) observed overshoots similar to the current study during unstable stratification conditions where the Obukhov length was measured as $L = -115$m. The Obukhov length was $L = -9$m during the current measurement period, i.e. the ABL was more unstable in comparison to Kunkel & Marusic (2006). Thus, the the observed overshoot could be expected.

3.2 Probability Distributions: Velocity Fluctuations, Acceleration and Vorticity

Figure 5 shows the probability distribution functions (PDF) for u', v' and w' normalized by U_τ. The markers indicate the measured distributions, while the curves represent Gaussian distributions fitted onto the results. The PDF of u' appears trimodal with a peak of 0 and two inflection points at $u' = \pm5$. The tri-modality may indicate that the PDF is not fully converged. However, the tri-modality may also have been caused by changes in the mean wind direction.

Besides the tri-modality of u', the experimental distri-

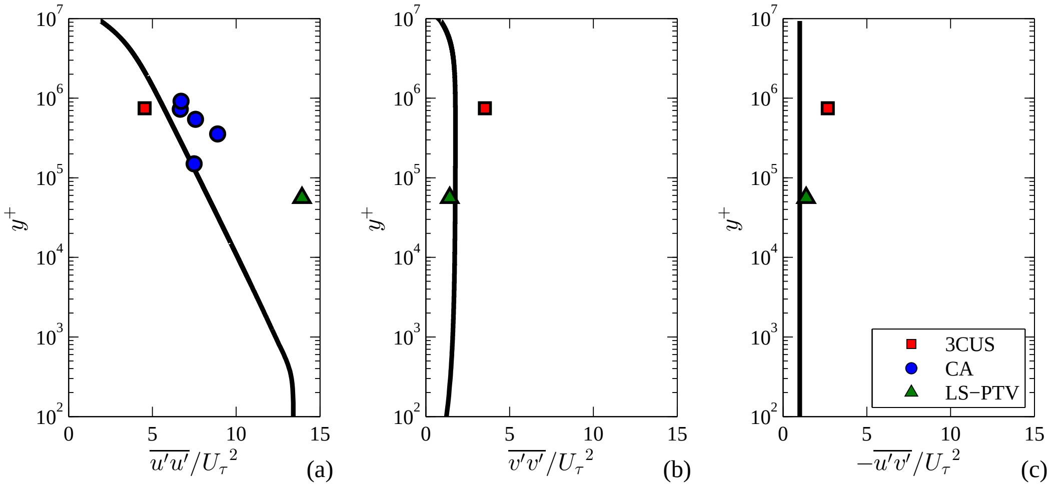

Figure 4: Streamwise (a), vertical (b) and shear (c) stresses normalized by $U_\tau{}^2$. The black curves represent similarity formulations developed in Marusic *et al.* (1997) and Kunkel & Marusic (2006), or $\overline{u'v'}/U_\tau{}^2 = -1$ in the case of (c) (Kaimal & Finnigan, 1994). The green-triangle markers indicate measurements taken by the LS-PTV system, while the red-square and blue-circle markers indicate ultrasonic- (3CUS) and cup-anemometer (CA) measurements, respectively.

butions appear to be Gaussian with u' exhibiting a larger variance than both v' and w'. Similar observations have been made from large eddy simulations of channel flows (Zhou *et al.*, 2005). To quantify how coincident a Gaussian distribution is with the experimental distributions, χ^2 tests were performed using twenty bins and a confidence level of 25% in a similar fashion to Zhou *et al.* (2005). The χ^2 values for the u', v' and w' distributions were 1181, 427 and 696, respectively, indicating they are not well described by a Gaussian distribution. Zhou *et al.* (2005) also observed χ^2 values on the order of 1000 and 100 for the u' and v' distributions, respectively. Zhou *et al.* (2005) postulated that the non-normal probability distributions exhibited by the velocity fluctuations are attributable to coherent structures present within the flow, which cause the velocity fluctuations to behave non-randomly.

As stated previously, unlike point measurements, the LS-PTV system can measure Lagrangian acceleration and vorticity of a particle. The PDFs for streamwise, normal and spanwise accelerations (a_x, a_y and a_z, respectively) are shown in Figure 6. The accelerations have been normalized by their respective standard deviations, $< a_i^2 >^{1/2}$. All three PDFs of acceleration agree with the parametrized probability distribution function for isotropic turbulence described in La Porta *et al.* (2001), in which the tails extend further outwards than a Gaussian distribution of equal variance. This suggests that acceleration is a highly intermittent variable and that extreme acceleration events are common. The fact that the distributions of all three acceleration components are well described by a single curve indicates that acceleration is an isotropic variable. La Porta *et al.* (2001) observed that acceleration became increasingly isotropic as the Taylor-microscale Reynolds number was increased from $Re_\lambda = 200$ to $Re_\lambda = 970$. The Taylor-microscale Reynolds number for the current study is estimated as $Re_\lambda \sim \mathscr{O}(10^4)$. Schroeder *et al.* (2011) also observed isotropic acceleration distributions in canonical TBL experiments performed at $Re_\theta = 2460$.

The PDFs for streamwise, normal and spanwise components of vorticity (ω_x, ω_y and ω_z, respectively) are plot-

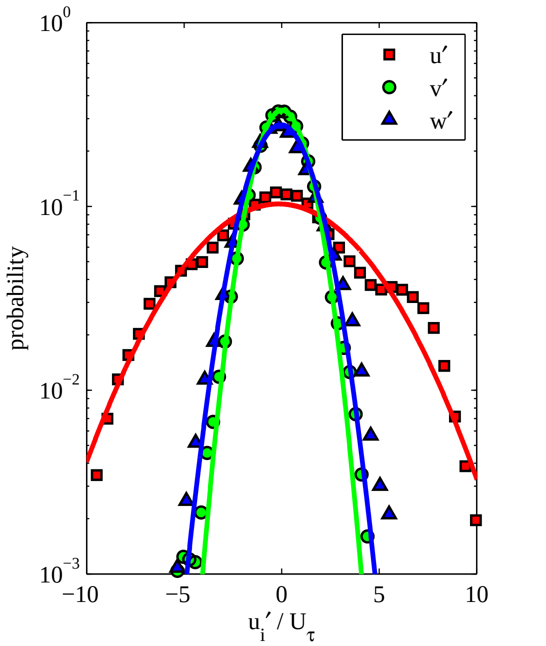

Figure 5: Probability distribution functions of u', v' and w' normalized by U_τ. The markers represent experimental results. The solid curves are fitted Gaussian distributions.

ted in Figure 8. Like the probability distributions for acceleration, the tails of the vorticity distributions extend outwards indicating that extreme events in vorticity are more prevalent than as predicted by a Gaussian curve. This can be quantified by the kurtosis of the distributions. Kurtosis represents the prevalence of extreme events relative to the mean of a PDF and is equal to the ratio of the fourth moment to the square of the variance. The streamwise, normal and vertical PDFs exhibit kurtosis values of 279, 121 and 147, respectively. In contrast, Gaussian distributions

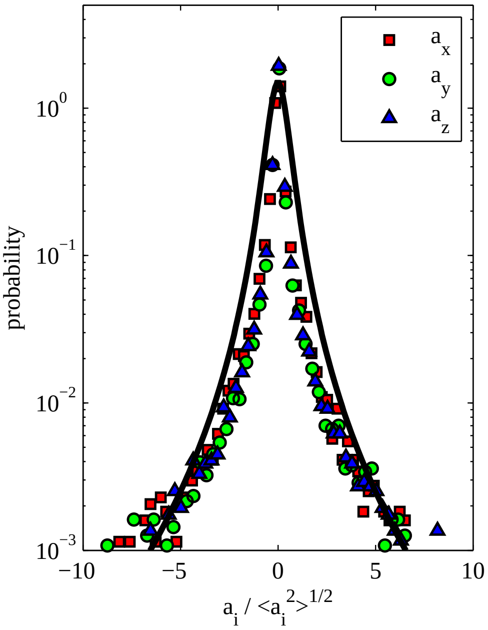

Figure 6: Probability distribution functions for a_x, a_y and a_z normalized by their respective standard deviation. The black curve is the parametrization for Lagrangian acceleration from La Porta *et al.* (2001).

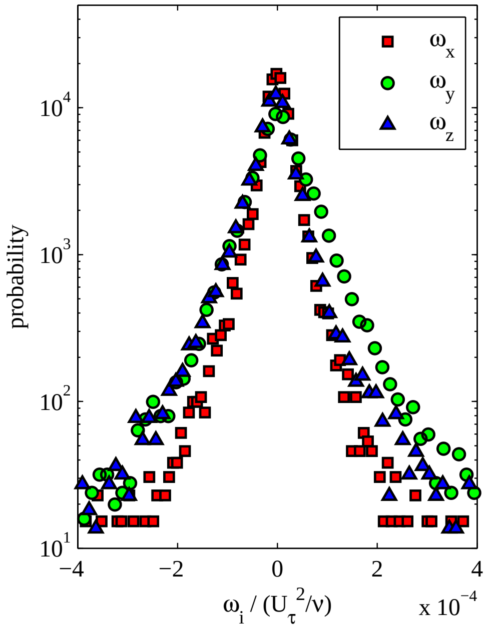

Figure 8: Probability distribution functions of ω_x, ω_y and ω_z normalized by the factor U_τ^2/ν. The markers represent experimental results.

have a kurtosis value of 0. In canonical TBL studies (Balint *et al.*, 1991; Honkan & Andreopoulos, 1997), the PDFs for all three vorticity components exhibited kurtosis values that would increase with distance from the wall. The kurtosis increased from $3 \sim 4$ at heights of $y^+ = 20$ to $6 \sim 8$ at heights of $y^+ = 80$. Thus, the kurtosis values of the current study are reasonable, considering the centre of the measurement volume was at a height of $y^+ = 5.6 \times 10^4$.

The objective behind the LS-PTV system is to quantify large-scale turbulent coherent structures found within canonical TBLs, such as hairpin vortices, within ABL flow. Ideally, the LS-PTV data would allow for the identification of *Lagrangian coherent structures* (LCS), which in three-dimensions are volumes delineated by material surfaces that either attract or repel particle paths (Haller, 2000). The LCS method has been shown to objectively identify hairpin vortices in channel flow whereas common Eulerian methods rely on arbitrary thresholds set by the experimenter (Green *et al.*, 2007). At present the measurement volume of the LS-PTV system is not sufficiently concentrated with tracer particles to perform such an analysis. Thus, the authors are working towards increasing the rate at which bubbles are produced by the manifold system. Meanwhile, the authors are developing a method to identify vortical structures from the geometry of particle paths that exhibit swirling motion. Examples of swirling paths are plotted in Figure 7. Particle-path geometry has been studied statistically (Braun *et al.*, 2006) but to the authors' knowledge, it has not been applied as a means of structure identification.

4 CONCLUSIONS

A large-scale particle tracking velocimetry (LS-PTV) system that tracks fog-filled soap bubbles has been presented as a means of characterizing coherent structures within the lower log region of the ABL. Wind measurements were taken over a volume of approximately 16m^3 centered 3m above the ground. The mean velocity and Reynolds stresses as measured by the LS-PTV system agreed well with measurements taken by a nearby wind-mast and a eddy-covariance system, as well as with Reynolds stress similarity formulations. The probability distribution functions of all three components of velocity fluctuations were normally distributed and centered about 0. Furthermore, the acceleration and vorticity probability distributions are exponential and symmetric about 0. The acceleration probability distributions were well described by the probability parametrization function from La Porta *et al.* (2001). The LS-PTV system can capture pathlines that exhibit a high degree of swirl, which can be potentially used to quantify vortical structures within the flow.

REFERENCES

2008 *Guide to Meteorological Instruments and Methods of Observation*, 7th edn. World Meteorological Organization.

Adrian, R. J. 2007 Hairpin vortex organization in wall turbulence. *Physics of Fluids* **19**.

Balint, J-L, Wallace, J. M. & Vukoslavcevic, P. 1991 The velocity and vortcity vector fields of a turbulent boundary layer. part 2. statistical properties. *Journal of Fluid Mechanics* **228**, 53–86.

Braun, W., de Lillo, F. & Eckhardt, B. 2006 Geometry of particle paths in turbulent flows. *Journal of Turbulence* **7** (62).

Fernholz, H. H. & Finley, P. J. 1996 The incompressible zero-preesure-gradient turbulent boundary layer: An assessment of the data. *Progress in Aerospace Sciences* **32**, 245–311.

Green, M. A., Rowley, C. W. & Haller, G. 2007 Detection of lagrangian coherent structures in three-dimensionl turbulence. *Journal of Fluid Mechanics* **572**, 111–120.

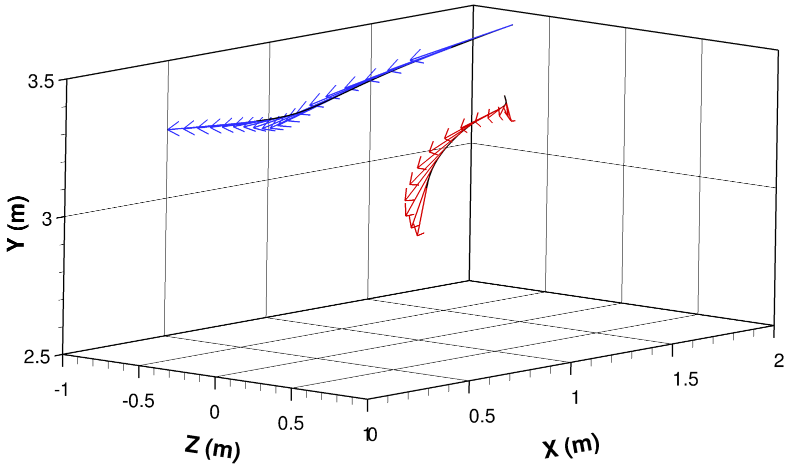

Figure 7: Examples of particle tracks exhibiting swirling motion. The arrows along the path indicate the direction of the flow.

Haller, G. 2000 Distinguished material surfaces and coherent structures in three-dimensional fluid flows. *Physica D* **149**, 248–277.

Hayashi, M., Jackson, J. F. & Xu, L. 2010 Application of the versatile soil moisture budget model to estimate evaporation from prarie grassland. *Canadian Water Resources Journal* **35** (2).

Hommema, S. E. & Adrian, R. J. 2003 Packet structure of surface eddies in the atmospheric boundary layer. *Boundary Layer Meteorology* **106**, 147–170.

Honkan, A. & Andreopoulos, Y. 1997 Vorticity, strain-rate and dissipation characteristics in the near-wall region of turbulent boundary layers. *Journal of Fluid Mechanics* **350**, 29–96.

Hutchins, N. & Marusic, I. 2007 Evidence of very long meandering features in the logarirthmic region of turbulent boundary layers. *Journal of Fluid Mechanics* **579**, 1–28.

Kaimal, J. C. & Finnigan, J. J. 1994 *Atmospheric Boundary Layer Flows–Their Structure and Measurement*. New York, NY: Oxford University Press.

Kunkel, G. J. & Marusic, I. 2006 Study of the near-wall-turbulent region of the high reynolds-number boundary layer using atmospheric flow. *Journal of Fluid Mechanics* **548**, 375–402.

La Porta, A., Voth, G. A., Crawford, A. M., Alexander, J. & Bodenschatz, E. 2001 Fluid particle accelerations in fully developed turbulence. *Lettes to Nature* **409**, 1017–1019.

Lüthi, B., Tsinober, A. & Kinzelbach, W. 2009 Lagrangian measurement of vorticity dynamics in a turbulent flow. *Journal of Fluid Mechanics* .

Marusic, I., Mathis, R. & Hutchins, N. 2010*a* High reynolds number effects in wall turbulence. *International Journal of Heat and Fluid Flow* **31**, 418–428.

Marusic, I., McKeon, B. J., Monkewitz, P. A., Nagib, H. M., Smits, A. J. & Sreenivasan, K. R. 2010*b* Wall-bounded turbulent flows at high reynolds numbers: Recent advances and key issues. *Physics of Fluids* **25**, 431–442.

Marusic, I., Uddin, A. K. M. & Perry, A. E. 1997 Similarity law for streamwise turbulence intensity in zero-pressure-gradient turbulent boundary layers. *Physics of Fluids* **9** (12).

McKeon, B. J. & Morrison, J. F. 2007 Asymptotic scaling in turbulent pipe flow. *Philosophical Transactions of the Royal Society A-Mathematical Physical and Engineering Sciences* **365**, 771–787.

Morris, S. C., Stolpa, S. R., Slaboch, P. E. & Klewicki, C. K. 2007 Near-surface particle image velocimetry measurements in a transitionaly rough-wall atmospheric surface layer. *Journal of Fluid Mechanics* **580**, 319–338.

Robinson, S. K. 1991 Coherent motions in the turbulent boundary layer. *Annual Review of Fluid Mechanics* **23**, 601–639.

Rosi, G. A., Martinuzzi, R. J. & Rival, D. E. in press A conditional analysis of spanwise vortices within the lower atmospheric log layer. *Journal of Wind Engineering and Industrial Aerodynamics* .

Scarabino, A., Sterling, M., Richards, P. J., Baker, C. J. & Hoxey, R. P. 2007 An investigation of the structure of ensemble averaged extreme wind events. *Wind and Structures* **10** (2), 135–151.

Schroeder, A., Geisler, R., Staack, K., Elsinga, G. E., Scarano, F., Wieneke, B., Henning, A., Poelma, C. & Westerweel, J. 2011 Eulerian and langrangian views of a turbulent boundary layer flow using time-resolved tomographic piv. *Experiments in Fluids* **50**, 1071–1091.

Smits, A. J., McKeon, B. J. & Marusic, I. 2011 High-reynolds number wall turbulence. *Annual Review of Fluid Mechanics* **43**, 353–375.

Wu, Y. & Christensen, K. T. 2006 Population trends of spanwise vortices in wall turbulence. *Journal of Fluid Mechanics* **568**, 55–76.

Zhou, J-F., Zhang, Q. & Li, J-C 2005 Probability distribution function of near-wall turbulent velocity fluctuations. *Applied Mathematics and Mechanics* **26** (10), 1245–1254.